Available online at www.sciencedirect.com
SCIENCE DIRECT®
International Journal of Heat and Mass Transfer 49 (2006) 3634–3644
International Journal of HEAT and MASS TRANSFER
www.elsevier.com/locate/ijhmt

Study on main flow and fuel injector configurations for Scramjet applications

Mohammad Ali *, A.K.M. Sadrul Islam

Department of Mechanical Engineering, Bangladesh University of Engineering and Technology (BUET), Dhaka 1000, Bangladesh

Received 25 April 2005; received in revised form 23 December 2005
Available online 18 April 2006

Abstract

A parametric study of combustor inlet configuration for supersonic combustion ramjet (Scramjet) engine has been conducted by solving two-dimensional full Navier–Stokes equations. The main stream is air of Mach 5 entering through the configured inlet of the combustor and gaseous hydrogen is injected from the configured jet on the side wall. The parameters included are air stream angle and injection angle. On the effect of air stream angle, strong interaction between main and injecting flows can be observed for smaller angle causing sharp increase in mixing efficiency on the top of injector. Also high momentum of air stream towards the side wall causes no recirculation at the upstream of injector and the system becomes unable for flame holding. For the variation of injection angle, results show that in upstream of injector the mixing is dominated by recirculation and in downstream the mixing is dominated by mass concentration of hydrogen. Upstream recirculation is dominant for injecting angle 60° and 90°. Incorporating the various effects, perpendicular injection shows the maximum mixing efficiency and its large upstream recirculation region has a good flame holding capability.

Keywords: Scramjet engine; TVD scheme; Backward-facing step; Supersonic mixing

1. Introduction

Mixing of fuel with oxidizer and their combustion are encountered in many engineering applications including hypersonic propulsion system in space vehicles. Particularly, the fuel injection scheme in hypersonic vehicles incorporating Scramjet engines requires special attention for efficient mixing and stable combustion. Though some of the researches have been carried out on mixing and combustion of fuel with oxidizer in Scramjet program, still it faces many unresolved problems. The main problems that arise in this regard concern mixing of reactants, ignition, flame holding, and completion of combustion. More investigations are required to overcome these problems. In fact, in supersonic combustion, high penetration and mixing of injectant with main stream is difficult due to their short residence time in combustor as described by Brown et al. [1] and Papamoschou et al. [2]. These investigations showed that good mixing and high penetration of injectant is difficult for the flow of high Mach number. Therefore, it is necessary to investigate the physical mechanisms that affect the mixing and combustion in Scramjet engine.

Several investigations have been performed to analyze the mixing and combustion characteristics, and find out the means of increasing the mixing efficiency. In these investigations the authors showed a number of parameters that can affect on penetration and mixing. In an experiment, Rogers [3] showed the effect of the ratio between jet dynamic pressure and freestream dynamic pressure on the penetration and mixing of a sonic hydrogen jet injected normal to a Mach 4 airstream. In similar flow arrangements, Kraemer et al. [4] found that the relative change in jet momentum was directly proportional to the relative size between the flowfield disturbance and the upstream separation distance. The downstream injectant penetration height is directly proportional to the upstream separation distance and thus, the downstream mixing is dependent

* Corresponding author.
E-mail address: mali@me.buet.ac.bd (M. Ali).

0017-9310/$ - see front matter © 2006 Elsevier Ltd. All rights reserved.
doi:10.1016/j.ijheatmasstransfer.2005.12.023

Nomenclature

c	sound speed (m/s)
C_p	specific heat at constant pressure (J/(kg K))
D_t	turbulent diffusion coefficient (m^2/s)
E	total energy (J/m^3)
F	flux vector in x-direction
$\hat{F}$	transformed flux vector in ξ-direction
G	flux vector in y-direction
$\hat{G}$	transformed flux vector in η-direction
H	enthalpy (J/kg)
J	transformation Jacobian
$\dot{m}$	mass flux of species (kg/s)
p	pressure (Pa)
q	energy flux by conduction (W/m^2)
R	universal gas constant (J/(kg mol K))
T	temperature (K)
u	horizontal velocity (m/s)
U	vector of conservative variables
$\hat{U}$	transformed vector of conservative variables
U	contravariant velocity in ξ-direction
v	vertical velocity (m/s)
V	contravariant velocity in η-direction
W	molecular weight of species (gm/mol)
x	horizontal cartesian coordinate (m)
Y	mass fraction of species
y	vertical cartesian coordinate (m)
θ	injecting angle (degree)
ψ	air inlet angle (degree)
ξ	transformed coordinate in horizontal direction
η	transformed coordinate in vertical direction
ρ	mass density (kg/m^3)
σ	normal stress (Pa)
τ	shear stress (Pa)
μ	coefficient of dynamic viscosity (kg/(m s))
κ	thermal conductivity (W/(m K))
δ	boundary layer thickness (m)
δ^*	kinematic displacement thickness (m)
ϕ'	local equivalence ratio of hydrogen and oxygen
Φ	global equivalence ratio of hydrogen and oxygen
φ	contour level

Superscript

ns	number of species

Subscripts

i, j	index for species
l	laminar case
m	mixture
t	index for turbulence
v	viscosity term
x	horizontal direction
y	vertical direction
xy	reference plane
0	reference value, stagnation condition

on the relative change in jet momentum. Weidner et al. [5] conducted a parametric study using staged, perpendicular fuel injectors. They studied the mixing of hydrogen by varying the distance between injectors and the fuel split (percentage of fuel injected per injector). Yokota et al. [6,7] examined the effects of injection methods, and the existence of pressure wave in the flow with the injection on mixing and total pressure loss. By the numerical investigation of two-dimensional reacting Scramjet engine flow fields, Drummond et al. [8] found that the insufficient penetration of hydrogen caused by locating the injector 6.0 cm from the engine minimum crosssection reduced the overall reaction in the upstream portion of combustor. Ali et al. [9] studied the mixing mechanisms and investigated mixing and combustion characteristics for several flow configurations. On the analysis of mixing the author observed that the backward-facing step in finite flow configuration plays an important role to enhance mixing and penetration in both upstream and downstream of injector. Investigation proved that without diffusion, injectant can spread in the flow field due to species continuity equations, but does not mix with main stream.

It can be pointed out that the air-breathing engines are important for the future hypersonic vehicles and the space planes. The concept of an airframe integrated Scramjet has evolved from NASA Langley Research Center [5] for hypersonic air-breathing engine. An engine module of the proposed Scramjet program consists of an air inlet, fuel injection struts and combustor as shown in Fig. 1 with sidewall removed. Several researchers including above conducted their investigations on many unresolved problems of Scramjet program, and much research remains to be done. In this study supersonic mixing and diffusion mechanisms of a hydrogen jet in two-dimensional finite air streams have been analyzed and discussed. Though the actual flow in a Scramjet combustor is three-dimensional, this paper investigates the two-dimensional flow to delineate the mechanisms of supersonic mixing for both main flow inlet and injector configurations. The geometric configuration of the calculation domain and the inlet flow conditions are shown in Fig. 2. The left boundary consists of a backward-facing step of height 5.0 mm under the inlet port of air which was found efficient in mixing by Ali et al. [10,11]. For this study, the air inlet angle 'ψ' is varied from 60°–120°, and the injection angle with side wall is varied from 30°–150°. The summary of computational runs is shown in Table 1. It can be pointed out that in eight cases, Cases 2 and 6 are of same configuration but for easy understanding these two cases are discussed separately in two varied parameters. For all cases the ratio of mass flow rate

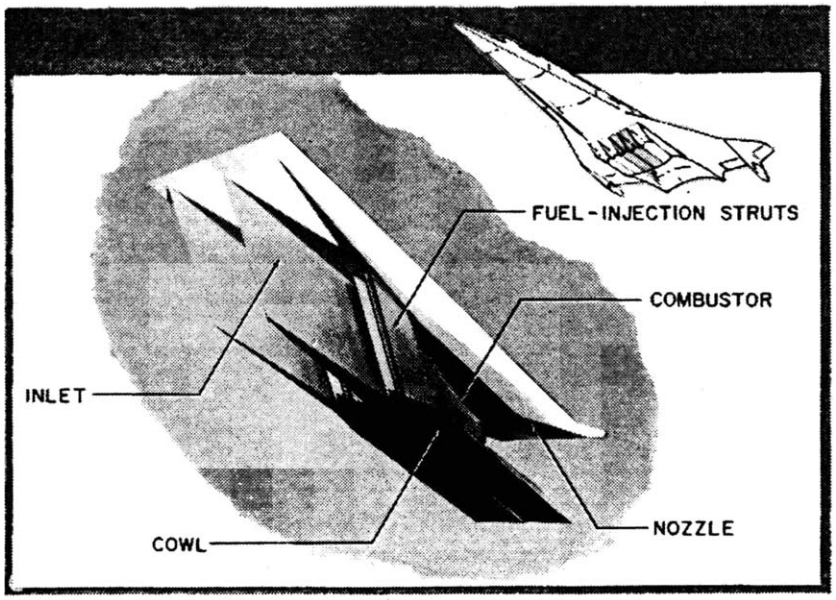

Fig. 1. A Scramjet engine module with removed side wall.

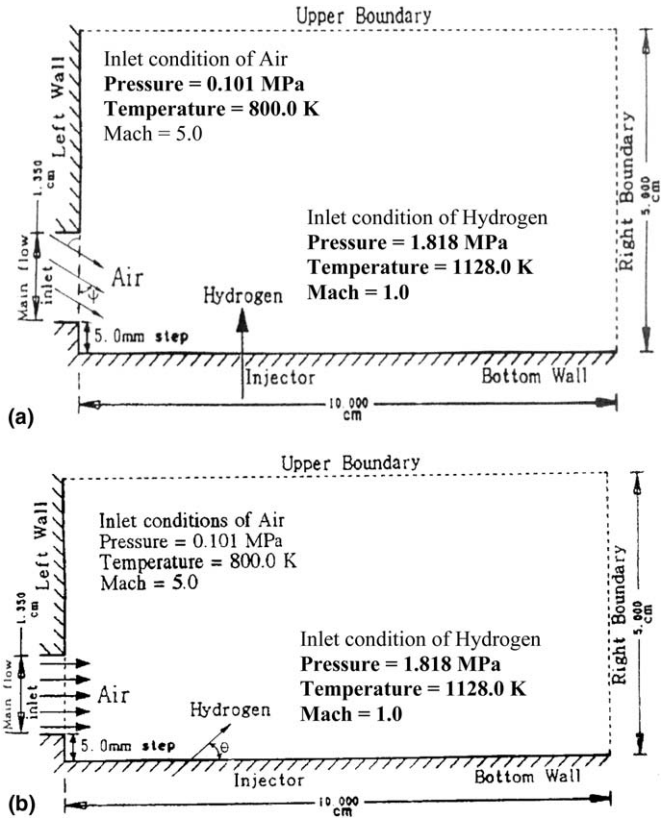

Fig. 2. Schematic of the physical model; (a) variation of air stream angle, (b) variation of injection angle.

between air stream and injected hydrogen, and total width of the combustor remain same. The inlet conditions of air are used as Weidner et al. [5] except Mach number. We choose the Mach 5.0 for the main flow as the test program has been conducted over the flight Mach number range [12] from 3.0 to 7.0.

Table 1
Summary of computational runs

Varying parameters	Computational runs (values of parameters)		Identification
	Air stream angle (ψ)	Injection angle (θ)	
Air stream angle (ψ)	60°	90°	Case 1
	90°	90°	Case 2
	120°	90°	Case 3
Injection angle (θ)	90°	30°	Case 4
	90°	60°	Case 5
	90°	90°	Case 6
	90°	120°	Case 7
	90°	150°	Case 8

2. Mathematical modeling

2.1. Governing equations

The flowfield is governed by the two-dimensional full Navier–Stokes equations with conservation equations of species. Body forces are neglected. For non-reacting flow, these equations can be expressed by

$$\frac{\partial U}{\partial t}+\frac{\partial F}{\partial x}+\frac{\partial G}{\partial y}=\frac{\partial F_{\mathrm{v}}}{\partial x}+\frac{\partial G_{y}}{\partial y} \tag{1}$$

where

$$U=\begin{pmatrix}\rho\\ \rho u\\ \rho v\\ E\\ \rho_i\end{pmatrix},\quad F=\begin{pmatrix}\rho u\\ \rho u^2+p\\ \rho uv\\ (E+p)u\\ \rho_i u\end{pmatrix},\quad G=\begin{pmatrix}\rho v\\ \rho uv\\ \rho v^2+p\\ (E+p)v\\ \rho_i v\end{pmatrix},$$

$$F_{\mathrm{v}} = \begin{pmatrix} 0 \\ \sigma_x \\ \tau_{xy} \\ \sigma_x u + \tau_{xy} v + q_x \\ \dot{m}_{ix} \end{pmatrix}, \quad G_y = \begin{pmatrix} 0 \\ \tau_{xy} \\ \sigma_y \\ \tau_{yx} u + \sigma_y v + q_y \\ \dot{m}_{iy} \end{pmatrix}.$$

$$p = \sum_{j=1}^{\mathrm{ns}} \rho_j R_j T = \sum_{j=1}^{\mathrm{ns}} \rho_j \frac{R}{W_j} T,$$

$$E = \sum_{j=1}^{\mathrm{ns}} \rho_j C_{pj} T - \sum_{j=1}^{\mathrm{ns}} \rho_j \frac{R}{W_j} T + \frac{\rho}{2}(u^2 + v^2).$$

The following terms are expressed as,

$$\sigma_x = \lambda\left(\frac{\partial u}{\partial x} + \frac{\partial v}{\partial y}\right) + 2\mu\left(\frac{\partial u}{\partial x}\right),$$

$$\sigma_y = \lambda\left(\frac{\partial u}{\partial x} + \frac{\partial v}{\partial y}\right) + 2\mu\left(\frac{\partial v}{\partial y}\right),$$

$$\tau_{xy} = \tau_{yx} = \mu\left(\frac{\partial u}{\partial y} + \frac{\partial v}{\partial x}\right),$$

$$q_x = \kappa\frac{\partial T}{\partial x} + \rho\sum_{j=1}^{\mathrm{ns}} D_j H_j \frac{\partial Y_j}{\partial x},$$

$$q_y = \kappa\frac{\partial T}{\partial y} + \rho\sum_{j=1}^{\mathrm{ns}} D_j H_j \frac{\partial Y_j}{\partial y},$$

$$\dot{m}_{ix} = \rho D_i \frac{\partial Y_i}{\partial x}, \quad \dot{m}_{iy} = \rho D_i \frac{\partial Y_i}{\partial y}, \quad \lambda = -\frac{2}{3}\mu.$$

The values of C_p and H are considered as functions of temperature and determined from the polynomial curve fitting developed by Moss [13]. Temperature is calculated by Newton–Raphson method. The coefficients of molecular viscosity μ and thermal conductivity κ of each species are determined by Sutherland formulae and those of gas mixture by Wilke's formulae available in White [14]. The effective molecular diffusion coefficient for each species is determined by the formula given in Reid et al. [15].

2.2. Turbulence model

A zero-equation algebraic turbulence model developed by Baldwin and Lomax [16] is used to simulate boundary layer separation, recirculation and shock-expansion regions near the injector. The model is patterned with modifications that avoid the necessity for finding the edge of the boundary layer. This has been very helpful because at the injection port and adjacent region it is difficult to define boundary layer thickness. According to the model the eddy viscosity μ_t is defined as

$$\mu_t = \begin{cases} (\mu_t)_{\mathrm{inner}} & y \leqslant y_{\mathrm{crossover}} \\ (\mu_t)_{\mathrm{outer}} & y > y_{\mathrm{crossover}} \end{cases} \tag{2}$$

where y is the normal distance from the wall and $y_{\mathrm{crossover}}$ is the smallest value of y at which the value of viscosity in the outer region becomes less than or equal to the value of viscosity in the inner region.

The viscosity in the inner region is given by

$$(\mu_t)_{\mathrm{inner}} = \rho l^2 |\omega| \tag{3}$$

The mixing length in the inner region l is expressed as

$$l = ky\lfloor 1 - \exp(-y^+/A^+)\rfloor \tag{4}$$

where

$$y^+ = \frac{\rho_{\mathrm{w}} u_\tau y}{\mu_{\mathrm{w}}} = \frac{\sqrt{\rho_{\mathrm{w}}\tau_{\mathrm{w}}}\, y}{\mu_{\mathrm{w}}} \tag{5}$$

For two-dimensional flow, the magnitude of the vorticity is given by

$$|\omega| = \sqrt{\left(\frac{\partial u}{\partial y} - \frac{\partial v}{\partial x}\right)^2} \tag{6}$$

For the outer region,

$$(\mu_t)_{\mathrm{outer}} = KC_{\mathrm{CP}}\rho F_{\mathrm{WAKE}} F_{\mathrm{KLEB}}(y) \tag{7}$$

where K is the Clauser constant, C_{CP} an additional constant, and

$$F_{\mathrm{WAKE}} = \min\left\{(y_{\max}F_{\max}), (C_{\mathrm{wk}} y_{\max} U_{\mathrm{dif}}^2 / F_{\max})\right\} \tag{8}$$

Here $F_{\max}$ is the maximum value of the function

$$F(y) = y|\omega|\lfloor 1 - \exp(-y^+/A^+)\rfloor \tag{9}$$

at each y station in the flow domain, and $y_{\max}$ is the y coordinate at which this maximum occurs. The function $F_{\mathrm{KLEB}}(y)$ is the Klebanoff intermittency factor given by

$$F_{\mathrm{KLEB}}(y) = \left[1 + 5.5\left(\frac{C_{\mathrm{KLEB}} y}{y_{\max}}\right)^6\right]^{-1} \tag{10}$$

U_{dif} is the difference between the magnitude of the maximum and minimum total velocity in the profile at a fixed x station, expressed as

$$U_{\mathrm{dif}} = \left(\sqrt{u^2 + v^2}\right)_{\max} - \left(\sqrt{u^2 + v^2}\right)_{\min} \tag{11}$$

where $\left(\sqrt{u^2 + v^2}\right)$ is taken to be zero along all x station.

The outer formulation (Eqs. (8) and (9)) can be used in wakes as well as in attached and separated boundary layer. The product $y_{\max}F_{\max}$ replaces $\delta^* u_{\mathrm{e}}$ in the Clauser formulation and the combination $y_{\max}U_{\mathrm{dif}}^2/F_{\max}$ replaces δU_{dif} in a wake formulation. In effect, the distribution of vorticity is used to determine length scales so that the necessity for finding the outer edge of the boundary layer is removed.

The following are the constants used for this model and are directly taken from Baldwin and Lomax [16]:

$$A^+ = 26, \quad C_{\mathrm{CP}} = 1.6, \quad C_{\mathrm{KLEB}} = 0.3, \quad C_{\mathrm{wk}} = 0.25,$$
$$k = 0.4, \quad K = 0.0168$$

The values of the turbulent thermal conductivity of the mixture κ_t and turbulent diffusion coefficient of ith species D_{it} are obtained from eddy viscosity coefficient μ_t by assuming a constant turbulent Prandtl and Lewis number

equal to 0.91 and 1.0, respectively. They can be expressed as

$$\frac{\mu_t C_p}{k_t} = 0.91 \tag{12}$$

$$\frac{\rho D_{it} C_p}{k_t} = 1.0 \tag{13}$$

The final values of μ, κ and D_{im} used in the governing equations are

$$\mu = \mu_l + \mu_t \tag{14}$$

$$\kappa = \kappa_l + \kappa_t \tag{15}$$

$$D_{im} = D_{iml} + D_{it} \tag{16}$$

2.3. Numerical scheme

The system of governing equations is solved using an explicit Harten-Yee Non-MUSCL Modified-flux-type TVD scheme [17]. The two-dimensional, rectangular physical coordinate system (x, y) is transformed into the computational coordinate system (ξ, η) in order to solve the problem on uniform grids. After applying the transformation, Eq. (1) can be expressed as

$$\frac{\partial \hat{U}}{\partial t} + \frac{\partial \hat{F}}{\partial \xi} + \frac{\partial \hat{G}}{\partial \eta} = \frac{\partial \hat{F}_v}{\partial \xi} + \frac{\partial \hat{G}_v}{\partial \eta} \tag{17}$$

where

$$\hat{U} = J^{-1}U, \quad \hat{F} = J^{-1}(\xi_x F + \xi_y G),$$
$$\hat{G} = J^{-1}(\eta_x F + \eta_y G), \hat{F}_v = J^{-1}(\xi_x F_v + \xi_y G_v),$$
$$\hat{G}_v = J^{-1}(\eta_x F_v + \eta_y G_v).$$

The grid Jacobian J and metric terms are

$$J^{-1} = x_\xi y_\eta - x_\eta y_\xi, \quad \xi_x = J y_\eta, \ \ \xi_y = -J x_\eta, \ \ \eta_x = -J y_\xi,$$
$$\eta_y = J_\xi.$$

For the left hand side of Eq. (17), the explicit Non-MUSCL TVD scheme can be written as

$$\hat{U}^{n+1}_{i,j} = \hat{U}^n_{i,j} - J_{i,j}\frac{\Delta t}{\Delta \xi}\left(\hat{F}^n_{i+1/2,j} - \hat{F}^n_{i-1/2,j}\right) - J_{i,j}\frac{\Delta t}{\Delta \eta}\left(\hat{G}^n_{i,j+1/2} - \hat{G}^n_{i,j-1/2}\right) \tag{18}$$

The variables $\hat{F}$ and $\hat{G}$ can be described as

$$\hat{F}^n_{i+1/2,j} = \frac{1}{2}\left(\hat{F}^n_{i,j} + \hat{F}^n_{i+1,j} + \hat{R}_{i+1/2}\hat{\Phi}_{i+1/2}\right) \tag{19}$$

The $\hat{R}_{i+1/2}$ is an eigen vector matrix and $\hat{\Phi}_{i+1/2}$ is a vector with the elements $\phi^l_{i+1/2}$ $(l = 1, 2, 3, 4, 5)$. The variables used in the above equations are

$$\hat{\Phi}_{i+1/2} = \left\{\hat{\Phi}^l{}_{i+1/2}\right\} = \left\{\sigma\left(\hat{a}^l{}_{i+1/2}\right)\left(\hat{g}^l{}_{i+1} + \hat{g}^l{}_i\right) - \psi\left(\hat{a}^l{}_{i+1/2} + \hat{\gamma}^l{}_{i+1/2}\right)\hat{\alpha}^l{}_{i+1/2}\right\} \quad l = 1\text{–}5 \tag{20}$$

$$\sigma(z) = \frac{1}{2}\left\{\psi(z) - \frac{\Delta t}{\Delta \xi}z^2\right\} \tag{21}$$

$$\psi(z) = \begin{cases} z; & |z| \geqslant \delta_l \\ \left(z^2 + \delta_l^2\right)/2\delta_l; & |z| < \delta_l \end{cases} \tag{22}$$

δ_l is a function that defines the range of entropy correction, and should be a function of the contravariant velocity and the corresponding sound speed for the computations. The form of the function used here is

$$\delta_l = \overline{\delta}\left(|U| + |V| + c\sqrt{\xi_x^2 + \xi_y^2 + \eta_x^2 + \eta_y^2}\right) \tag{23}$$

with a constant $\overline{\delta}$ set to 0.15. More details about the scheme can be found in Yee [18].

The minmod limiter, simplified form of which can be found in Yee [18], was used to avoid the numerical oscillations at the discontinuity. Among the various approximate Riemann solvers [18], we used the Roe's average which is the most common one due to its simplicity and ability to return to the exact solution whenever the variables lie on a shock or contact discontinuity.

3. Boundary conditions and convergence criterion

A Navier–Stokes analysis imposes that the normal and tangential velocity components are zero on the walls. The walls are assumed to be thermally adiabatic, so that $(\partial T/\partial n)_w = 0$. For non-catalytic walls, the normal derivative of species mass fraction also vanishes, and consequently the gradient of total density becomes zero. The pressure is determined from the equation of state. The temperature, pressure and density at inflow boundary are assumed steady. At outflow boundary the variables are determined by first-order extrapolation due to supersonic character of flow. Throughout the present study, the following convergence criterion has been set on the variation of density:

$$\sqrt{\frac{\sum_{J=1,K=1}^{JJ,KK}\left(\frac{\rho_{new}-\rho_{old}}{\rho_{old}}\right)^2}{JJ \cdot KK}} \leqslant 10^{-5}$$

where JJ and KK are the total number of nodes in the horizontal and vertical directions, respectively.

4. Results and discussion

4.1. Program verification

To verify the present code, a comparison has been made with the experimental data published by Weidner et al. [5]. The geometry of the experiment is shown in the inset on Fig. 3, where helium was injected at sonic condition from a 0.0559 cm slot into a rectangular duct of 25.4 cm long and 7.62 cm high. The slot was located 17.8 cm downstream of the duct entrance. The flow conditions of helium at the slot exit were $P = 1.24$ MPa, $T = 217.0$ K and

$M = 1.0$. At the entrance of the duct, the airstream conditions were $P = 0.0663$ MPa, $T = 108.0$ K and $M = 2.9$. Using the same geometry and flow conditions we computed the flowfield with a grid system consisting of 246×165 nodes in the horizontal and vertical directions, respectively. At the exit of the injector 10 nodal points are used.

Results are given in Figs. 3–5. Fig. 3 shows that the computed pressure along the bottom wall agrees well with the experiment in both the upstream and downstream of the injector. Both show a pressure rise in the upstream separated region and downstream reattachment region. An over-prediction can be found at the immediate downstream of the injector where the turbulence is naturally intensified by the disturbance caused by the injector. Fig. 4 gives the static pressure distribution along the vertical axis at 3.81 cm downstream of the injector. Qualitatively, the computed pressure profile agrees with the experimental data. Small variation on the position of recompression shock and bow shock, and the pressures at these positions can be observed in the computation. In the experiment, the

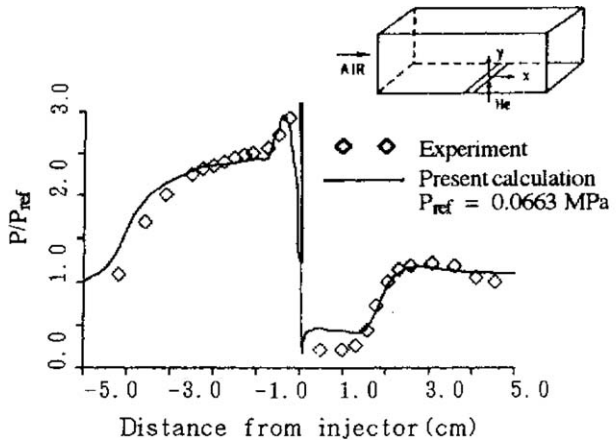

Fig. 3. Comparison between experimental and computed pressures along bottom wall.

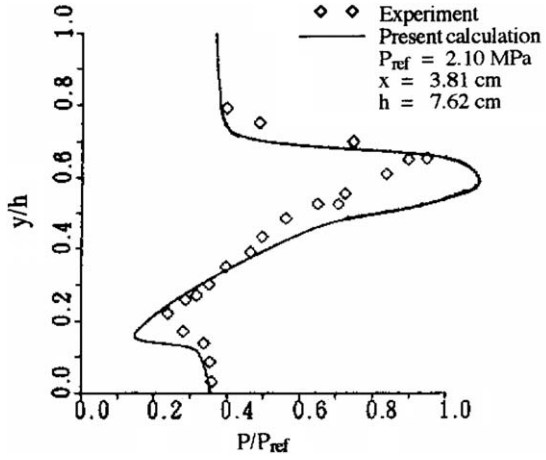

Fig. 4. Comparison between experimental and computed pressures at 3.81 cm downstream of injector.

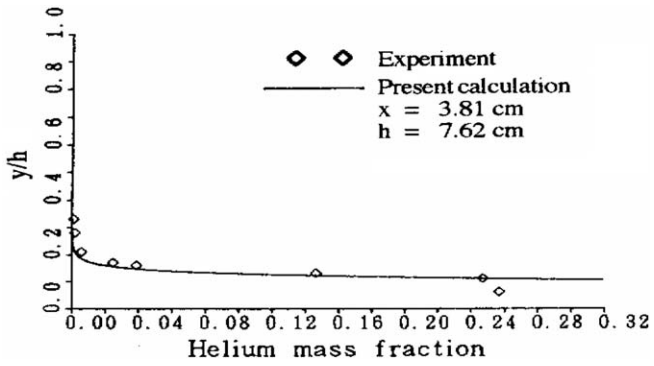

Fig. 5. Comparison among helium mass fraction at 3.81 cm downstream of injector.

recompression shock occurs at $y/h = 0.2$ (h is the height of domain), whereas in computation at 0.16. After recompression, both show a linear increase of pressure. The calculation determines the similar difference in the position of bow shock as that of recompression shock. In the experiment the position of bow shock is at $y/h = 0.63$, while in computation it is 0.59. Beyond the bow shock, the calculation shows the similar decreasing rate of pressure with experiment. Fig. 5 shows the comparison between the mass fraction profiles of injected helium along the same vertical axis at 3.81 cm downstream of the injector. The computed curve agrees with the experimental data at all points along the vertical axis.

The computation shows that the overall computed results agree with the experiment in spite of the complexities of injected flow field. The code is therefore considered to be adequate for application to calculate the mixing flow fields.

4.2. Effect of inlet air angle

The velocity in upstream of injector, penetration and diffusion of hydrogen, and mixing efficiencies of different cases have been analyzed and discussed. Fig. 6 shows the velocity vector in both upstream and downstream of injector for the variation of inlet air angle. For Case 1 ($\psi = 60°$), the free air stream strikes the wall near injector with a high momentum. At the region of striking there is a strong interaction between the main flow and the side jet, and the flow is deflected at an angle more than 60° in the upward direction. Due to strike of the main flow at upstream region with high momentum, there is no recirculation in upstream of injector. Case 3 ($\psi = 120°$) shows that the interaction between the main flow and injecting hydrogen is weak and there is no upstream recirculation for this case as the main flow deflects upward after weak interaction with the side jet. In downstream there is no recirculation in Cases 1–3. Another observation is that for Case 2 ($\psi = 90°$) the injecting jet plume expands towards upstream due to the backward facing step which increases the thickness of hydrogen-air mixing layer. Fig. 7 shows the penetration and mass concentration of hydrogen in the flow field. There

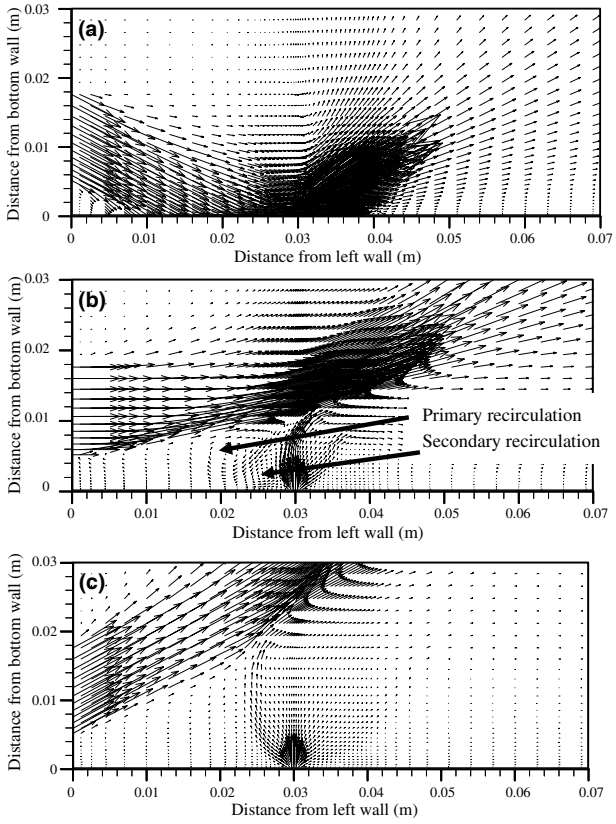

Fig. 6. Velocity vector around the injector; (a) Case 1, (b) Case 2, and (c) Case 3.

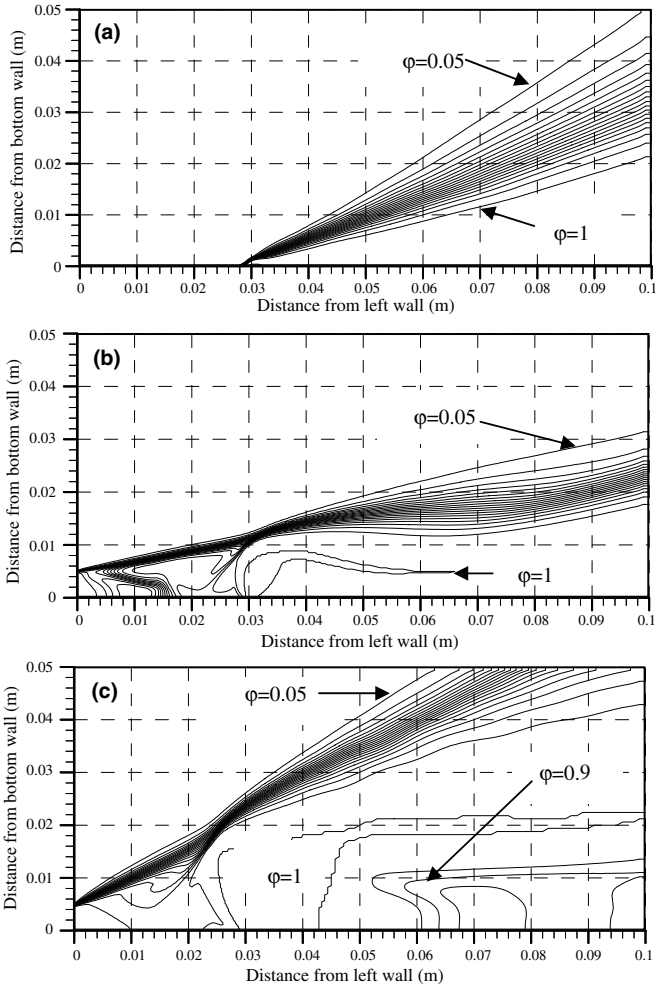

Fig. 7. Mole fraction contours of hydrogen, $\phi =$ contour levels ranges from 0.05 to 0.95 with an increment of 0.05; (a) Case 1, (b) Case 2, and (c) Case 3.

are various definitions of "penetration" in the literature. In this paper the term "penetration" is referred to the edge of mixing region in the vertical direction where the mole fraction of hydrogen is 5%. Different penetration of hydrogen at both upstream and downstream among the configurations can be found. In Case 1 we see that there is no hydrogen in upstream of the injector because a high momentum main flow strikes the wall near the injector resulting in no recirculation at that region and then deflects away at an angle more than 60° with the horizontal direction. We know that recirculation is an important factor for mixing of hydrogen with air in upstream region and as there is no recirculation, no mixing of hydrogen and air in upstream of the injector occurs. Due to primary and secondary upstream recirculations, Fig. 7(b) indicates that there is good mixing between air and hydrogen in upstream of the injector. Again we know that the flame holding requires longer residence time of flame in the burning range and this residence time strongly depends on the geometric expansion of the recirculation zone [19]. Accordingly Case 2 has a good flame holding capability because it can produce larger and elongated upstream recirculation where most of the region contains better proportion of hydrogen and oxygen. For high inlet air angle in Case 3, expansion of hydrogen is high in both upstream and downstream as shown in Fig. 7(c) which causes high concentration of hydrogen especially in upstream and eventually low flame holding capability. Due to high expansion of hydrogen, the flow becomes slower and very small amount of air reaches to the wall by diffusion making hydrogen mole fraction 0.9 as shown in Fig. 7(c).

The performance of different cases is evaluated by calculating mixing efficiency. Mathematically, the mixing efficiency is defined by

$$\eta_m = \frac{\int_A (f_H \rho \vec{u}\, d\vec{A})/\phi'}{\dot{m}_H/\Phi}$$

where

A	arbitrary section plane
f_H	local mass fraction of hydrogen
ρ	total density
$\vec{u}$	velocity vector
$d\vec{A}$	small area normal to velocity vector
$\dot{m}_H$	total mass flux of hydrogen
ϕ'	local equivalence ratio $= \begin{cases} 0.25 & \phi' < 0.25 \\ \phi' & \phi' \geqslant 0.25 \end{cases}$

Physically mixing efficiency indicates the ratio of hydrogen mass flow rate capable of burning to its total mass flow rate at the exit of side jet. In the flow field where large amount of hydrogen is present with negligible amount of oxygen, the calculation of mixing efficiency is avoided by dividing the large value of ϕ'. On the other hand, where a very small amount of hydrogen is present, an error in calculation of mixing efficiency can be occurred by the small value of ϕ'. This error has been eliminated by setting the minimum value of $\phi' = 0.25$ which corresponds to the lower flammability limit. It can be mentioned that Yokota et al. [6,7] used similar expression for calculating mixing efficiency in the flow field. In this investigation, the global equivalence ratio for all cases is $\Phi = 2$. The mixing efficiency along the combustor length is shown in Fig. 8, which shows that mixing efficiency increases sharply at injector position of respective cases. Generally in upstream region the increasing rate of mixing is moderate and in downstream it is very slow. The reason is that in upstream hydrogen mixes with air by both recirculation and diffusion, and in downstream mixing is occurring only by diffusion. In recirculation hydrogen has much time to mix with air, whereas in downstream the flow is supersonic and has little time for diffusion. Individually Case 1 has the highest increment of mixing efficiency at injector position due to large gradient of mass concentration and the mixing efficiency up to 0.03 m from left boundary is zero. Because of high momentum of air stream, there is no hydrogen in upstream of the injector which makes the mixing efficiency zero. Case 3 has no increment of mixing efficiency in downstream of injector which indicates that the unnecessary increasing of combustor length in far downstream will only increase the material cost for construction. In downstream, the increasing rate of mixing is slower for all cases caused by the supersonic nature of flow. However, among the cases investigated, Case 1 has the maximum increasing rate of mixing in downstream due to high expansion of hydrogen.

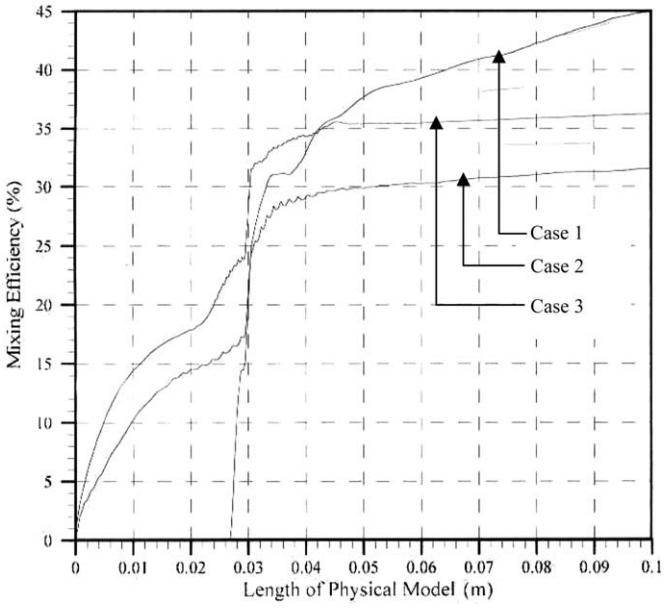

Fig. 8. Mixing efficiency along the length of physical model (Cases 1–3).

4.3. Effects of injection angle

Fig. 9(a)–(e) show the velocity vector in both upstream and downstream of injector. A pair of recirculation regions formed at the upstream of the injector, one of which is large and the other is small in size. In Case 4 the

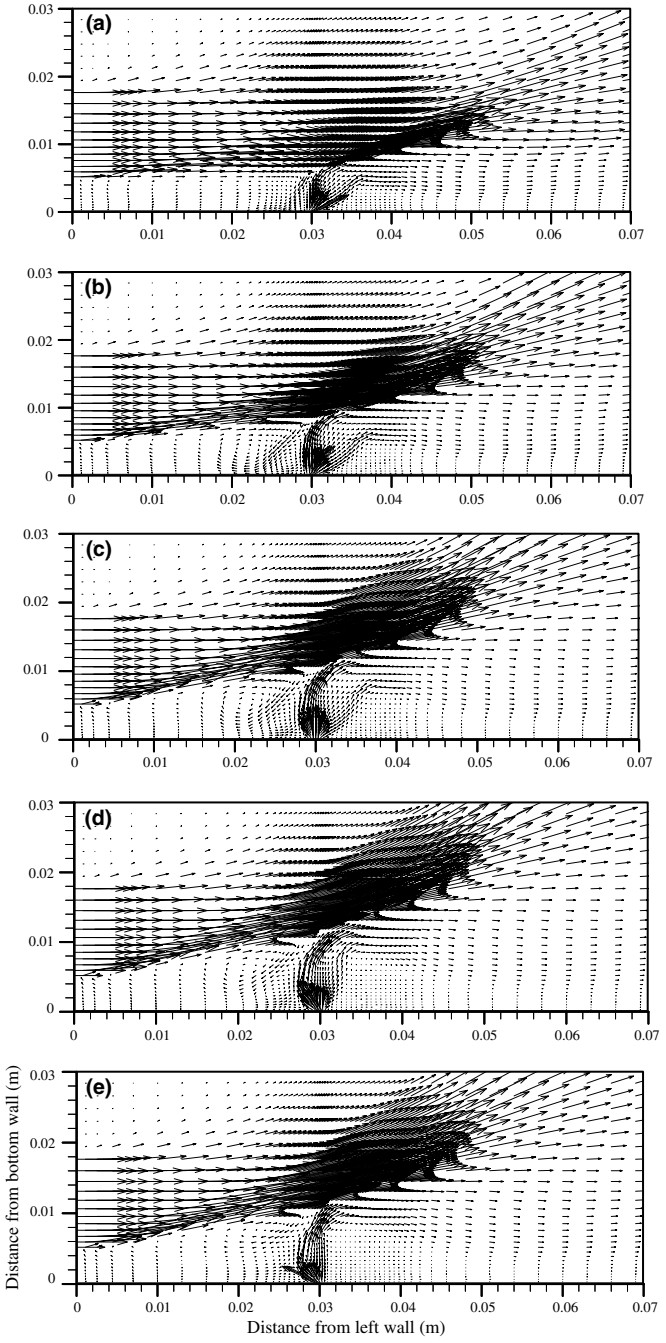

Fig. 9. Velocity vector near injector; (a) Case 4, (b) Case 5, (c) Case 6, (d) Case 7, and (e) Case 8.

recirculations are weak, which can be understood by the vector length in recirculation region. The increase of injection angle makes the recirculations stronger which can be found in Cases 5 and 6. For further increase of injecting angle, i.e., in Cases 7 and 8 they are not significant. The large primary clockwise recirculation is caused by the backward facing step and the secondary small counter-clockwise recirculation close to injector is caused by the primary recirculation and the suction of injection. The primary recirculation increases the boundary layer thickness and the injection into a thick boundary layer causes greater penetration resulting in higher mixing. Due to interaction between main flow and side jet, the velocity of main flow decreases and the air enters the upstream recirculation. On the other hand, by diffusion and convection due to injection, the injected hydrogen enters the recirculation and mixes well with air. So upstream recirculations play a vital role on mixing and consequently Cases 6 and 7 show better mixing. In downstream there is no strong recirculation in any case. Case 6 shows a very small recirculation just downstream of the injector caused by the suction of the injection and bending of the side jet. This recirculation and convection due to injection cause better mixing in Case 6.

Fig. 10(a)–(e) show the penetration and mass concentration of hydrogen in the flow field. In this figure φ indicates the contour level of hydrogen mole fraction. The value of the minimum contour level is 0.05 and that of the maximum contour level is 1.0. The increment of adjacent higher contour level is 0.05. It can be pointed out that the penetration and mixing of hydrogen in a numerical simulation can occur by means of (i) turbulence and convection due to recirculation, (ii) molecular diffusion, and (iii) numerical diffusion. It can be pointed out that numerical diffusion for mixing is an over prediction in such kind of investigation. Therefore, conducting a grid refinement study, Ali et al. [9] showed that mixing by numerical diffusion was not occurring in present flow field. The backward facing step associated with upstream recirculation brings the injected hydrogen up to the left boundary in all cases. The hydrogen penetration height at different downstream locations can be compared from Fig. 10(a)–(e). For example, at 10 cm from left boundary the penetration height is up to 2 cm in Case 4, whereas, it is 2.5 cm for Case 5 and above 3 cm for Cases 6 and 7. The penetration height of the hydrogen is higher in Cases 6 and 7 (above 3 cm) indicating more uniform distribution of hydrogen and consequently higher mixing efficiency. For all cases, i.e., Cases 4–8 the mole fraction contours of hydrogen are concentrated in a narrow region on the top of the injector, as shown in Fig. 10(a)–(e), which might become a high heat release zone in the reacting flowfield. The flame holding requires longer residence time of flame which depends on the geometric expansion of the recirculation zone. Also the equivalence ratio of fuel and oxidizer in mixture is an important factor for burning because among the mixtures, the stoichiometric mixture strength is good for combustion.

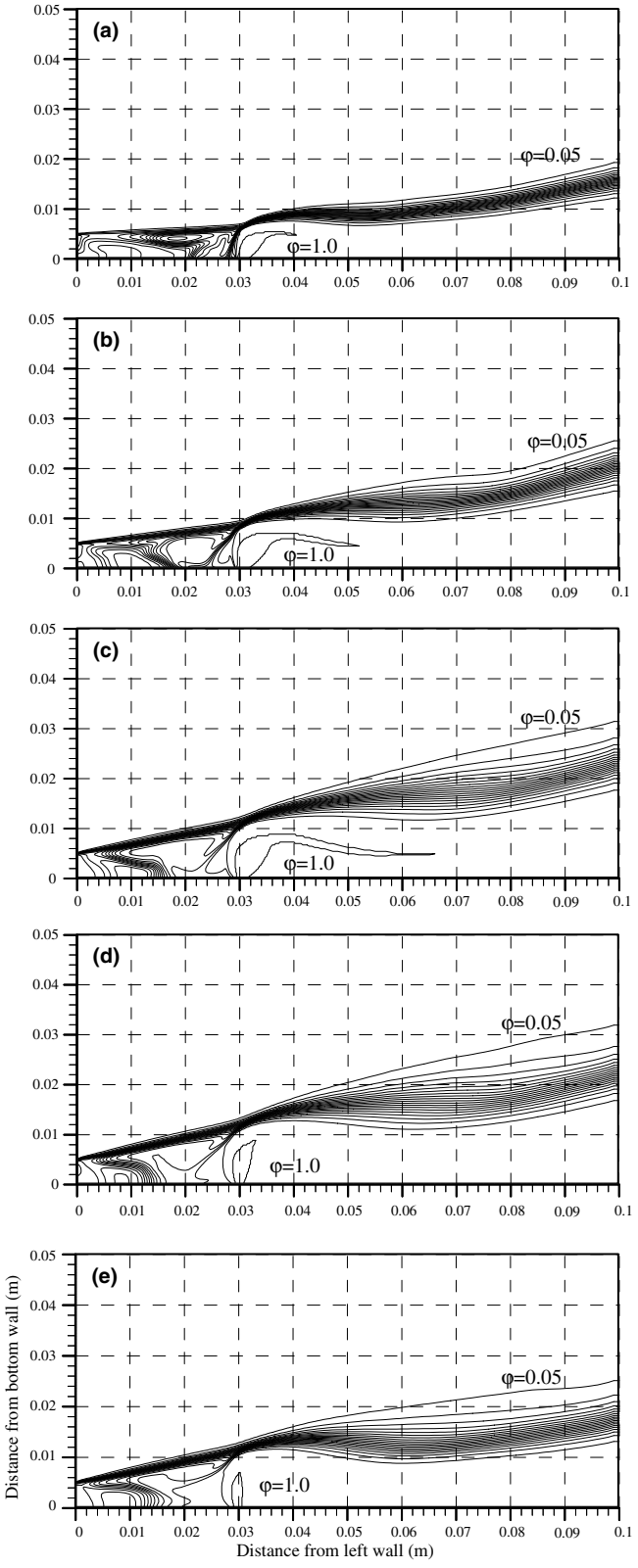

Fig. 10. Mole fraction contour of Hydrogen, $\varphi(0.05, 1.0)$; φ is contour level, (a) Case 4, (b) Case 5, (c) Case 6, (d) Case 7, and (e) Case 8.

Therefore, longer recirculation zone containing stoichiometric mixture strength results in a longer residence time and

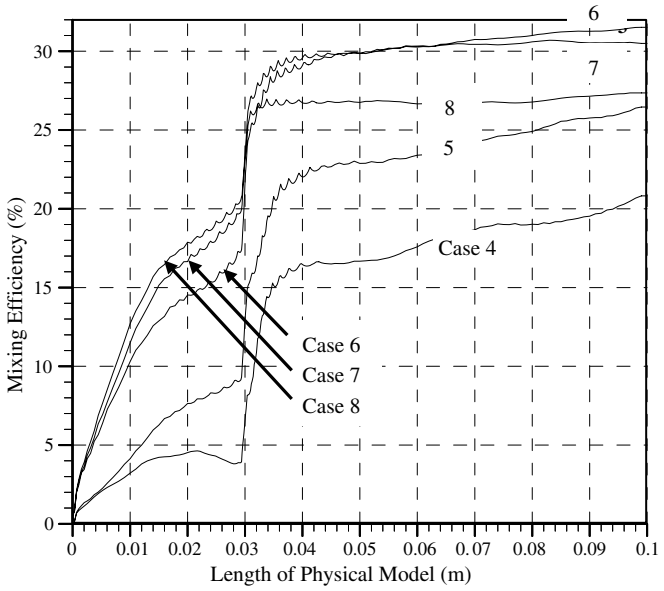

Fig. 11. Mixing efficiency along the length of physical model (Cases 4–8).

leads to a more stable flame. Accordingly Cases 6 ($\theta = 90°$) and 7 ($\theta = 120°$) have good flame holding capability, because they can produce larger and elongated upstream recirculation where stoichiometric mixture area is larger. Again in cases having $\theta = 30°$ and 150° upstream region contains lower mass concentration of hydrogen which is not good for flame holding. In downstream hydrogen distribution is seemed to be better in Cases 6 and 7 as mentioned earlier because of higher expansion of side jet.

The performance of different cases is evaluated by calculating mixing efficiency. Fig. 11 shows that mixing efficiency increases sharply at injector position caused by high mass concentration of hydrogen. In general, the increasing of mixing is moderate in upstream region and in downstream it is very slow. Individually, Case 6 ($\theta = 90°$) and Case 7 ($\theta = 120°$) have the highest value of mixing efficiency (28%) at injector position due to strong upstream recirculation. In downstream the increasing rate of mixing along the length of physical model for Case 6 ($\theta = 90°$) is higher than Case 7 ($\theta = 120°$), whereas, for Case 8 ($\theta = 150°$) it remains almost constant which indicates that very long combustor might increase the construction cost for Case 8 provided the other parameters are identical. Among the cases considered in this investigation two competing phenomena about the mixing can be observed: (i) in upstream mixing is dominated by recirculation and (ii) in downstream it is dominated by hydrogen mass concentration. Due to larger recirculation in upstream of injector hydrogen mixes well with oxygen in Cases 6–8 indicating higher mixing efficiency. In downstream Cases 4 and 5 show higher increasing rate of mixing due to higher mass concentration of hydrogen. However, mixing efficiency increased by recirculation in Cases 6–8 can not be recovered in Cases 4 and 5 by increasing rate of mixing efficiency dominated by hydrogen mass concentration in downstream. Finally, we can see that Case 6 shows the maximum mixing efficiency (31.5%) at the right end of calculation domain.

5. Conclusions

The present paper gives some information on mixing of fuel with oxidizer and flame holding capability of the combustion flow field due to variation of air stream angle and injection angle. It is found that the air stream of smaller angle shows higher mixing efficiency but has no recirculation in upstream of injector, which is much important for flame holding capability. On the other hand, higher angle of air stream causes higher expansion of the side jet and the upstream of injector is seemed to be stagnant. For the variation of injection angle, two competing phenomena were observed: (i) in upstream of injector mixing efficiency was dominated by convection due to recirculation and (ii) in downstream mixing efficiency was dominated by mass concentration of hydrogen. Incorporating all the effects the configuration of injection angle 90° has the maximum mixing efficiency and its upstream recirculation region with good proportion of hydrogen and oxygen might act as a good flame holder in Scramjet combustor.

References

[1] G.L. Brown, A. Roshko, On density effects and large structure in turbulent mixing layer, J. Fluid Mech. 64 (4) (1974) 575–816.
[2] D. Papamoschou, A. Roshko, Observation of Supersonic Free Shear Layers, AIAA Paper, 1986, 86-0162.
[3] R.C.A. Rogers, Study of the Mixing of Hydrogen Injected Normal to a Supersonic Airstream, NASA TN, 1971, D-6114.
[4] G.O. Kraemer, S.N. Tiwari, Interaction of Two-Dimensional Transverse Jet with a Supersonic Mainstream, NASA CR, 1983, 175446.
[5] E.H. Weidner, J.P.A. Drummond, Parametric Study of Staged Fuel Injector Configurations for Scramjet Applications, AIAA Paper, 1981, 81-11468.
[6] K. Yokota, S. Kaji, The Three-dimensional supersonic flow and mixing fields with a perpendicular air injection from a finite length slit, Trans. Jpn. Soc. Aero. Space Sci. 39 (124) (1996) 173–183.
[7] K. Yokota, S. Kaji, The effects of aspect ratio of a finite length slit on the mixing in the three-dimensional supersonic flow, Trans. Jpn. Soc. Aero. Space Sci. 39 (124) (1996) 199–210.
[8] J.P. Drummond, E.H. Weidner, Numerical Study of a Scramjet Engine Flow Field, AIAA Paper, 1981, 81-0186.
[9] M. Ali, T. Fujiwara, A. Parvez, A numerical study on the physics of mixing in two-dimensional supersonic stream, Indian J. Eng. Mater. Sci. 9 (2002) 115–127.
[10] M. Ali, T. Fujiwara, J.E. Leblanc, The effects of backward-facing step on mixing and flame holding in supersonic combustor, J. Energ. Heat Mass Transfer 23 (2001) 319–338.
[11] M. Ali, T. Fujiwara, Penetration and mixing of hydrogen injected normal to a two-dimensional parallel supersonic flow, Trans. Jpn. Soc. Aero. Space Sci. 40 (130) (1997) 248–261.
[12] V.L. Rausch, C.R. McClinton, J.W. Hicks, Scramjet breath new life into hypersonics, Aerospace Am. (July) (1997) 40–46.
[13] J.N. Moss, Reacting Viscous-Shock-Layer Solutions with Multicomponent Diffusion and Mass Injection, NASA TR, 1974, 411.
[14] F.M. White, Viscous Fluid Flow, McGraw-Hill, New York, 1974.
[15] R.C. Reid, T.K. Sherwood, The Properties of Gases and Liquids, second ed., McGraw-Hill, New York, 1966, pp. 520–543.

[16] B.S. Baldwin, H. Lomax, Thin Layer Approximation and Algebraic Model for Separated Turbulent Flows, AIAA Paper, 1978, 78-257.
[17] H.C. Yee, A Class of High-Resolution Explicit and Implicit Shock Capturing Methods, NASA TM, 1989, 101088.
[18] H.C. Yee, Upwind and Symmetric Shock-Capturing Schemes, NASA TM, December 1990, 89464.
[19] S.J.U.Y. Tabejamaat, T. Niioka, Numerical simulation of secondary combustion of hydrogen injected from preburner into supersonic airflow, AIAA J. 35 (9) (1997) 1441–1447.